Nature of Catalytic Active Sites Present on the Surface of Advanced Bulk Tantalum Mixed Oxide Photocatalysts

Somphonh P. Phivilay,[†] Alexander A. Puretzky,[‡] Kazunari Domen,[§] and Israel E. Wachs*,[†]

[†]*Operando* Molecular Spectroscopy & Catalysis Laboratory, Department of Chemical Engineering, Lehigh University, Bethlehem, Pennsylvania 18015, United States

[‡]Center for Nanophase Materials Sciences and Materials Science and Technology Division, Oak Ridge National Laboratory, Oak Ridge, Tennessee 37831, United States

[§]Department of Chemical System Engineering, University of Tokyo, 7-3-1 Hongo, Bunkyo-ku, Tokyo 113-8656, Japan

(S) Supporting Information

ABSTRACT: The most active photocatalyst system for water splitting under ultraviolet (UV) irradiation (270 nm) is the promoted 0.2% $NiO/NaTaO_3$:2% La photocatalyst with an optimized photonic efficiency of 56%, but fundamental issues about the nature of the surface catalytic active sites and their involvement in the photocatalytic process still need to be clarified. This is the first study to apply cutting-edge surface spectroscopic analyses to determine the surface nature of tantalum mixed oxide photocatalysts. Surface analysis with high-resolution X-ray photoelectron spectroscopy (1−3 nm) and high-sensitivity

low-energy ion scattering spectroscopy (0.3 nm) indicates that the NiO and La_2O_3 promoters are concentrated in the surface region of the bulk $NaTaO_3$ phase. The NiO is concentrated on the $NaTaO_3$ outermost surface layers, while La_2O_3 is distributed throughout the $NaTaO_3$ surface region (1−3 nm). Raman and UV−vis spectroscopy revealed that the bulk molecular and electronic structures, respectively, of $NaTaO_3$ were not modified by the addition of the La_2O_3 and NiO promoters, with La_2O_3 resulting in a slightly more ordered structure. Photoluminescence spectroscopy reveals that the addition of La_2O_3 and NiO produces a greater number of electron traps resulting in the suppression of the recombination of excited electrons and holes. In contrast to earlier reports, La_2O_3 is only a textural promoter (increasing the BET surface area by ~7-fold by stabilizing smaller $NaTaO_3$ particles) and causes an ~3-fold decrease in the specific photocatalytic TOR_s (micromoles of H_2 per square meter per hour) rate because surface La_2O_3 blocks exposed catalytic active $NaTaO_3$ sites. The NiO promoter was found to be a potent electronic promoter that enhances the $NaTaO_3$ surface-normalized TOR_s by a factor of ~10−50 and turnover frequency by a factor of ~10. The level of NiO promotion is the same in the absence and presence of La_2O_3, demonstrating that there is no promotional synergistic interaction between the NiO and La_2O_3 promoters. This study demonstrates the important contributions of the photocatalyst surface properties to the fundamental molecular/electronic structure−photoactivity relationships of promoted $NaTaO_3$ photocatalysts that were previously not appreciated in the literature.

KEYWORDS: photocatalyst, $NaTaO_3$, NiO, La_2O_3, spectroscopy, photocatalysis, H_2O splitting
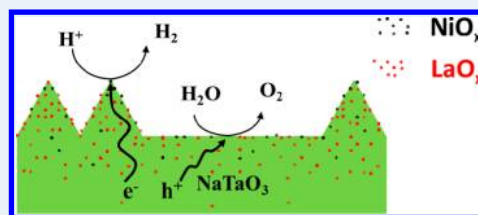
1. INTRODUCTION

Photocatalytic water splitting is a thermodynamically challenging reaction requiring a large positive change in the Gibbs free energy (238 kJ/mol) to produce H_2 fuel and molecular O_2. This phenomenon was first illuminated by the pioneering work of Fujishima and Honda in 1972,[1] and research efforts since then have focused on finding highly active metal oxide semiconductor materials for photocatalytic hydrogen production by water splitting. Hydrogen is considered to be one of the potential candidates to replace fossil fuel for our sustainable energy needs, especially if it can be generated from the photocatalytic conversion of cheap and abundant water into clean non-carbon hydrogen from solar energy resources. Development of this clean, renewable form of energy will help to address our reliance on depleted fossil fuel supplies and the environmental problems accompanying their use. Many metal oxide semiconductor catalysts (>130) are able to photocatalytically convert water into H_2 and O_2.[2−5] Semiconductor catalysts based on d^0 (Ti, Zr, Nb, Ta, and W) transition metal oxides and d^{10} (Ga, In, Ge, Sn, and Sb) main group metal oxides have emerged as candidates for use in heterogeneous photocatalytic systems because of their advantageous electronic configurations of empty/filled d orbitals that minimize trapping of excited electrons and holes. Although photocatalytic water splitting has garnered much interest in academia, there has not been much industrial interest in photocatalytic water splitting because of the low photocatalytic activity and the lack of extensive studies on industrial scale-up for the process.[5] Among the discovered semiconductor photocatalyst systems, tantalum-based photocatalysts such as

Ta_2O_5,[6,7] $NaTaO_3$,[8] $K_3Ta_3Si_2O_{13}$,[9] $SrTa_2O_6$,[10] and Na-TaO_3:La[11,12] have been found to be among the most promising for photocatalytic water splitting because of their high photoactivity under ultraviolet (UV) irradiation.

Some of the strategies employed to increase the activity of the photocatalysts include the addition of a cocatalyst such as NiO, Pt, Rh_2O_3, or RuO_2 as well as doping of the photocatalysts with metal ions to induce morphological changes.[13] These catalyst design strategies led to the discovery of lanthanum-doped $NaTaO_3$ loaded with a NiO cocatalyst (NiO/$NaTaO_3$:La), which is currently the most active photocatalyst for water splitting under UV irradiation at 270 nm with an optimized photonic efficiency of 56% and a stability of more than 400 h.[11] Bulk characterization techniques [X-ray diffraction (XRD), transmission electron microscopy (TEM), X-ray absorption near edge structure (XANES), and extended X-ray absorption fine structure (EXAFS)] suggested that LaO_x and NiO species are present as highly dispersed species on the surface of the catalysts because separate crystalline phases of NiO and LaO_x were not detected in the optimized photocatalysts. Electron microscopy revealed that the particle size of $NaTaO_3$:La (0.1–0.7 μm) is much smaller than that for undoped, La-free $NaTaO_3$ (2–3 μm), and ordered nanostep structures were also found to be present only on the smaller $NaTaO_3$:La particles.[11] It was proposed that the active sites for H_2 evolution are the highly dispersed NiO sites selectively deposited on the edges of the nanostep structures while the active site for O_2 evolution is at the groove of the nanostep structures. The high photoactivity of the catalysts was attributed to the spatial separation between the oxidative and reductive catalytic active sites. Deriving a model for the catalytic active surface sites based only on bulk characterization techniques is highly problematic because the surface of bulk mixed metal oxides can be enriched or depleted of one or more of its constituent components.[14,15] Thus, it is necessary to understand the nature of the surface region (~1–3 nm) and especially the outermost surface layer (~0.3 nm) of a photocatalyst because the catalytic chemical processes responsible for splitting H_2O into H_2 and O_2 occur via catalytic surface phenomena. This fundamental piece of information is critical in developing fundamentally sound photocatalytic models involving the catalytic active surface sites.

This is the first study to report on the surface nature of tantalum mixed oxide photocatalysts. This study will utilize cutting-edge surface spectroscopic analysis [high-resolution X-ray photoelectron spectroscopy (HR-XPS) and high-sensitivity low energy ion scattering (HS-LEIS) spectroscopy] to provide information about the nature of the surface region (~1–3 nm) and outermost atomic layer (~0.3 nm) of the photocatalysts where the catalytic active sites are located, respectively. The surface studies will be complemented by *in situ* optical spectroscopic characterization [Raman, UV–vis, photoluminescence (PL), and time-resolved picosecond PL–Raman] that provide further insight into the bulk molecular and electronic structure of $NaTaO_3$ photocatalysts and how the addition of NiO and La_2O_3 promoters affects these bulk properties. Time-resolved infrared (IR) spectroscopy has previously been utilized to examine the dynamics of photoexcited electrons of the NiO/NaTaO3:La photocatalyst (>100 ns),[16] which is on the time scale for the catalytic surface reaction.[17] The recombination of electron–hole pairs occurs much faster than that (pico- to nanoseconds), and time-resolved PL spectroscopy will be used in this study to examine emission decay kinetics on that time

scale. The objectives of this study are (i) to examine the roles of the surface and bulk characteristics of bulk mixed oxide semiconductor photocatalysts for water splitting and (ii) to establish fundamental structure–photoactivity relationships for the highly active tantalum-based photocatalysts.

2. EXPERIMENTAL SECTION

2.1. Photocatalyst Synthesis. The bulk $NaTaO_3$ and the doped $NaTaO_3$:La photocatalysts were synthesized by solid-state reactions.[11] Ta_2O_5 (HC Starck, ceramic grade), Na_2CO_3 (Aldrich, 99.5%), and La_2O_3 (Alfa Aesar, 99.99%) were mixed together and calcined at 1170 K for 1 h in air followed by intermediate grinding at ambient temperatures and then calcined in air at 1420 K for 10 h. The Na:La:Ta molar ratio was $1 - X$:X:1, with an excess amount of sodium (5% mol) used to compensate for the volatility of Na. The optimized doping of 2 mol % lanthanum was used in this study. The NiO (0.2 wt %) was subsequently added to the photocatalyst by impregnation of an aqueous solution of $Ni(NO_3)_2 \cdot 6H_2O$ (Aldrich, 99.999%). The powdered photocatalyst was placed into a porcelain crucible and heated over a water bath, and the suspension was stirred using a glass rod until the solution was completely evaporated. The dried powder was then mildly calcined at 540 K in air for 1 h.

2.2. *In Situ* Raman Spectroscopy. The Raman spectra of the photocatalysts were obtained on a Lab Ram-HR Raman spectrometer (Horiba-Jobin Yvon) equipped with visible (532 nm) laser excitation utilizing a confocal microscope (Olympus BX-30) for focusing the laser on the catalyst sample. The visible laser excitation was generated with a Nd:YAG laser (10 mW), with the scattered photons directed into a single monochromator and focused onto a UV-sensitive liquid N_2-cooled charge-coupled device (CCD) detector (Horiba-Jobin Yvon CCD-3000V) having a spectral resolution of ~2 cm^{-1} for the given parameters. Approximately 5–10 mg of the catalyst was placed into a high-temperature *in situ* cell (Linkam TS-1500) with a quartz window and cooled with flowing water. The catalyst samples were treated at 673 K for 1 h in a flowing 10% O_2/He mixture (Airgas, 30 mL/min) to desorb the adsorbed moisture, and the spectra of the dehydrated samples were recorded after the catalysts had been cooled to 373 K in the flowing 10% O_2/He gas to ensure that the catalyst surface was void of moisture. The spectral acquisition time employed for five scans was 5 s/scan for each spectrum (25 s/spectrum). System alignment was verified using a silica reference standard line at 520.7 cm^{-1}.

2.3. *In Situ* UV–Visible (UV–vis) Diffuse Reflectance Spectroscopy. The UV–vis diffuse reflectance spectra were recorded using a Varian Cary 5E UV–vis spectrophotometer with a diffuse reflectance attachment (Harrick Praying Mantis Attachment, DRA-2). The finely ground powder catalyst samples (~20 mg) were loaded into an *in situ* cell (Harrick, HVC-DR2) and measured in the 200–800 nm spectral region with a magnesium oxide reflectance standard used as the baseline. The UV–vis spectra of the photocatalysts were obtained after the samples had been treated at 673 K for 1 h in a flowing 10% O_2/He mixture (Airgas, 30 mL/min) to desorb the adsorbed moisture. Below 300 nm, the absorbance signal was unacceptably noisy and a filter (Varian, 1.5 ABS) was employed to minimize the background noise. The Kubelka–Munk function, $F(R_\infty)$, was determined from the UV–vis DRS absorbance and processed with Microsoft Excel. The UV–vis edge energy (E_g) was determined by finding the intercept of

the straight line in the low-energy rise of a plot of $[F(R_\infty) h\nu]^{1/n}$, where $n = 0.5$ for the direct allowed transition versus $h\nu$, where $h\nu$ is the energy of the incident photon.[18−20]

2.4. Photoluminescence (PL) Spectroscopy and Time-Resolved (TR) PL Spectroscopy. Photoluminescence spectra and lifetime emission decay were obtained using a tunable Ti:sapphire laser (Mira 900, Coherent), generating 5 ps pulses with a 76 MHz repetition rate and pumped with a frequency-doubled Nd:YVO$_4$ laser (Coherent Verdi V-18) set at 267 nm, and were directed into a tunable Raman−photoluminescence system (Jobin Yvon Horiba, T64000) with a UV objective lens to focus the laser onto the sample. Approximately 5−10 mg of the catalyst sample was placed into a high-temperature *in situ* cell (Linkam TS-1500) with a quartz window and cooled with flowing water. The cell was pretreated at 673 K by a flowing 10% O$_2$/N$_2$ mixture for 30 min to desorb adsorbed moisture and then cooled to 298 K in flowing N$_2$ where the photoluminescence spectrum was recorded. The emission spectrum was recorded in the 366−700 nm range, but contributions from the quartz window below 450 nm provided reliable PL spectra only above 450 nm. The PL emission spectra were normalized to the emission peak from the quartz window (∼406 nm) to account for PL intensity variations of the experimental setup. The peak of the PL spectrum was then used as the emission decay window for TR-PL lifetime measurements. For lifetime decay experiments, the luminescence light was subsequently backscattered through the objective lenses and focused onto a slit of a triple monochromator equipped with a fast gated intensified charge-coupled device (ICCD) camera (Picostar HR12, LaVision). The gate width was set to 500 ps, and the maximal delay was determined by the repetition rate of the Ti:sapphire laser (∼13200 ps). The laser energy at the sample was maintained at approximately 20 mW to prevent laser-induced sample damage. The experimental decay curves were first fit to a simple first-order exponential decay model:

$$y = A_1 \exp\left(\frac{-t}{t_1}\right) + y_0 \tag{1}$$

A double first-order exponential decay "biexponential" model was also used to account for the case in which the photoluminescence decay can be described as the decay of two different excited species back to their ground states independent of one another:[21,22]

$$y = A_1 \exp\left(\frac{-t}{t_1}\right) + A_2 \exp\left(\frac{-t}{t_2}\right) + y_0 \tag{2}$$

2.5. High-Resolution X-ray Photoelectron Spectroscopy (HR-XPS). The HR-XPS spectra of the surface region (∼1−3 nm) of the catalysts were obtained on a Scienta ESCA 300 spectrometer equipped with a 300 mm hemispherical electrostatic analyzer and a monochromatic Al Kα X-ray source with an energy of 1486.6 eV generated from a rotating anode. This allows for improved chemical selectivity by narrowing the spectral peaks of elements and greatly reducing the magnitude of the spectral background signal compared to that of conventional XPS spectrometers. Each spectrum was calibrated using a binding energy (BE) of 285.0 eV for carbon in the C1s region. The atomic concentration ratios were calculated by correcting the measured peak area ratios with relative sensitivity factors employed in Casa XPS version 2.3.15.

2.6. High-Sensitivity Low-Energy Ion Scattering (HS-LEIS) Spectroscopy. Analysis of the outermost surface layer (∼0.3 nm) of the photocatalysts was conducted with the Qtac100 HS-LEIS spectrometer (ION-TOF) equipped with a highly sensitive double toroïdal analyzer, with a sensitivity 3000-fold higher than that of conventional LEIS spectrometers, which allows for quantitative static depth profiling up to 10 nm. The photocatalyst samples were first gently cleaned with atomic oxygen to remove surface hydrocarbon contamination from the atmosphere prior to being transferred inside the analysis chamber. The HS-LEIS spectra were collected using both 3000 eV He$^+$ with a 8600 pA current and 4000 eV Ne$^+$ with a 2830 pA current as ion sources. For depth profiling, the surface was sputtered with 1000 eV Ar$^+$ at a sputter yield of 1×10^{15} ions/cm^2 corresponding to ∼1 surface layer (0.4 nm)/cycle.

3. RESULTS

3.1. *In Situ* Raman Spectroscopy. The *in situ* Raman spectra of the tantalum-based photocatalysts are shown in Figure 1. The Raman bands of the bulk Ta$_2$O$_5$ are indicative of
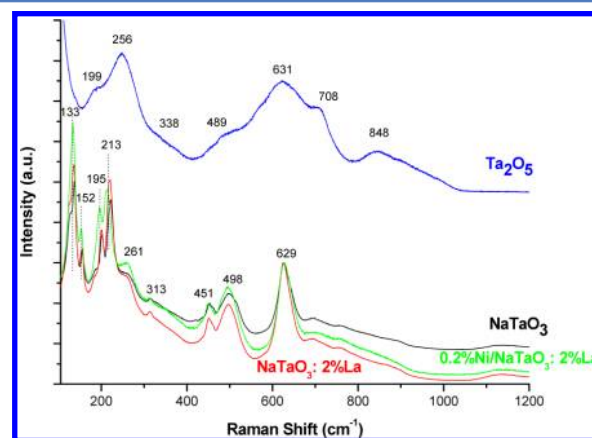
Figure 1. Raman spectra of tantalum-based photocatalysts with intensity normalized against Raman bands between 629 and 631 cm^{-1}.

the crystalline Ta$_2$O$_5$ (L) phase.[23] The largest band in the spectrum for the Ta$_2$O$_5$ (L) phase is at 100 cm^{-1}, originating from a lattice phonon mode along with the band at 199 cm^{-1}. The Raman bands at 256 and 338 cm^{-1} have been assigned to Ta−O−Ta and TaO$_6$ bending modes, respectively. The bands at 489, 631, 708, and 848 cm^{-1} are assigned to Ta−O−Ta symmetric stretching, Ta−O symmetric stretching, Ta−O−Ta antisymmetric stretching, and higher-order Ta−O symmetric stretching modes, respectively.[23]

The solid-state synthesis between Na$_2$CO$_3$ and Ta$_2$O$_5$ greatly changes the bulk crystal structure of the photocatalyst, and the Raman spectrum for the undoped NaTaO$_3$ photocatalyst is shown in Figure 1. Unmodified NaTaO$_3$ contains Raman bands at 133, 152, 195, and 213 cm^{-1} that can be assigned to Na translational vibration modes.[24] The bands at 261 and 313 cm^{-1} can be assigned to bending modes for TaO$_6$, and the bands at 451, 498, and 629 cm^{-1} can be assigned to Ta−O stretching modes. Doping of NaTaO$_3$ with La and Ni does not result in any apparent changes in the Raman features of NaTaO$_3$:La and NiO/NaTaO$_3$:La relative to those of NaTaO$_3$, suggesting that addition of the dopants has a minimal effect on the crystallinity of NaTaO$_3$ (Na−O and Ta−O vibrations below and above 250 cm^{-1}, respectively). Crystalline La$_2$O$_3$ bands (104, 191, and 411 cm^{-1})[25] are not detected, indicating

that La_2O_3 is present as an amorphous or highly dispersed phase in the $NaTaO_3$:La photocatalyst. The crystalline NiO vibrations, broad overlapping bands at 460 and 500 cm^{-1}, are not detected because of their relatively weak Raman bands[26] or because of the presence of dispersed NiO species. Thus, the bulk molecular structure of $NaTaO_3$ does not appear to be perturbed by the addition of the lanthanum and nickel oxide dopants.

3.2. *In Situ* UV–Vis Diffuse Reflectance Spectroscopy.

The *in situ* UV–vis DRS Eg values for the tantalum-based photocatalysts are listed in Table 1. The bulk band gap energies

Table 1. Optical Edge Energy (Eg) Values from UV–vis DRS

catalyst	Eg (eV)
Ta_2O_5	4.1 ± 0.1
$NaTaO_3$	4.2 ± 0.1
0.2% $NiO/NaTaO_3$	4.2 ± 0.1
$NaTaO_3$:2% La	4.2 ± 0.1
0.2% $NiO/NaTaO_3$:2% La	4.2 ± 0.1

are comparable for all the tantalum-based photocatalysts within experimental error and are in agreement with previously reported Eg values in the literature.[7,11] The addition of the La_2O_3 and NiO promoters does not affect the band gap energy for $NaTaO_3$, reflecting its dominant contribution to the band gap for the promoted $NiO/NaTaO_3$:La photocatalyst.

3.3. PL and Time-Resolved PL (TR-PL) Spectroscopy.

PL emission spectroscopy monitors recombination of photo-excited electrons and holes of a material. The photoluminescence emission spectra with 267 nm excitation for the tantalum-based photocatalysts are presented in Figure 2. The
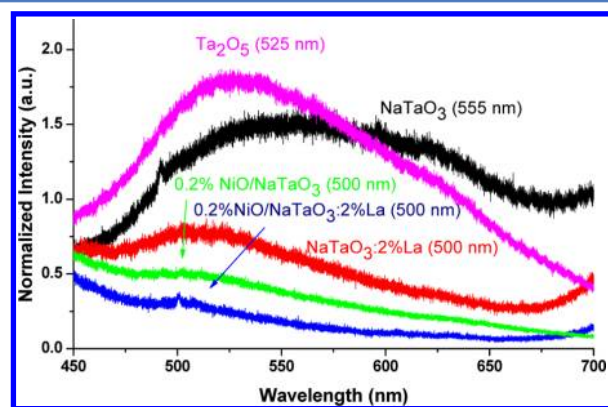
Figure 2. PL spectra with 267 nm excitation for tantalum-based photocatalysts with peak maxima in parentheses.

bulk Ta_2O_5 photocatalyst exhibits a very intense and broad peak with a maximum at 525 nm. The PL spectrum of the

undoped $NaTaO_3$ is much broader with a maximum at 555 nm. The intense PL emissions reflect the ability of these bulk phases to generate electron–hole pairs and their subsequent recombination under continuous light excitation that is responsible for the PL emission. The addition of the La_2O_3 and NiO promoters to $NaTaO_3$ results in the suppression of the PL emission intensity, suggesting that these promoters are helping to prevent electron–hole recombination in the bulk $NaTaO_3$ phase.

The PL decay curves obtained via TR-PL spectroscopy for the tantalum photocatalysts are plotted in Figure S1 of the Supporting Information. The emission decays for the tantalum-based photocatalysts were modeled with eqs 1 and 2, and the fit parameters are listed in Table 2. The bulk Ta_2O_5 photocatalyst was found to fit the simple first-order exponential decay model, while the $NaTaO_3$ photocatalysts fit the biexponential model. The observed simple first-order exponential decay model for the bulk Ta_2O_5 catalyst can be attributed to the homogeneity of this bulk catalyst, where the emission decay is dominated by only one type of excited tantalum species decaying back to the ground state.[21] This single-species decay is not seen in the $NaTaO_3$ photocatalysts where multiple excited species exist and decay back to their ground states independently of each other. Two different regimes in the decay curves can be observed for the $NaTaO_3$ photocatalysts that are identified as the "fast" component of decay, which dominates at early decay times, and the "slow" component of the decay, which dominates at later decay times. Parameters t_1 and t_2 refer to the decay times for the fast and slow components, respectively, and A_1 and A_2 are the decay constants that refer to the amplitudes of the fast and slow components, respectively.

The PL emission decay is related to the lifetimes of the photogenerated electron–hole pairs, with slower decay rates indicating longer lifetimes.[27,28] The decay time for Ta_2O_5 is on the same time scale as the slow component of decay of the $NaTaO_3$ photocatalysts. The larger value for decay time t_2 for $NaTaO_3$ is indicative of longer decay lifetimes compared to that of Ta_2O_5. For modified $NaTaO_3$ photocatalysts, the addition of either La_2O_3 or NiO leads to a decrease in the decay time of the fast component (t_1) with a concurrent increase in the decay constant (A_1) of the fast component. For the slow component (t_2), however, addition of NiO yields a modest decrease in the decay time (t_2) and decay constant (A_2), while addition of La_2O_3 leads to an increase in the decay time (t_2) and a decrease in the decay constant (A_2). The addition of 0.2% NiO to $NaTaO_3$:La has the most dramatic effect on the PL response. For the fast component, the decay constant increases by a factor of ~10^6 and the decay time slightly decreases, while for the slow component, the decay time decreases by an order of magnitude and the decay constant increases. The net effect of adding the La_2O_3 and NiO promoters to $NaTaO_3$ is that the contribution of the fast component (A_1) to the overall PL

**Table 2. TR-PL Decay Fit Parameters[a] for Catalysts with 267 nm Excitation**

catalyst	t_1 (ns)	A_1	t_2 (ns)	A_2	$A_1/(A_1 + A_2)$	$A_2/(A_1 + A_2)$
Ta_2O_5	0.00	0.00	5.0	3.5	0.00	1.0×10^0
$NaTaO_3$	0.80	1.9×10^2	17	3.6	0.98	1.9×10^{-2}
0.2% $NiO/NaTaO_3$	0.52	4.8×10^2	10	2.8	0.99	5.9×10^{-3}
$NaTaO_3$:2% La	0.34	2.7×10^4	42	2.8	≥0.99	1.0×10^{-4}
0.2% $NiO/NaTaO_3$:2% La	0.15	1.4×10^{10}	3.5	5.0	≥0.99	3.6×10^{-10}

[a] $y = A_1 \exp(-t/t_1) + A_2 \exp(-t/t_2) + y_0$.

response spectra becomes more dominant [see $A_1/(A_1 + A_2)$ values in Table 2] and the slow component decay time significantly decreases when NiO is added [see $A_2/(A_1 + A_2)$ values in Table 2].

3.4. High-Resolution X-ray Photoelectron Spectroscopy.

HR-XPS was employed to determine the elemental composition of the surface region ($\sim$1$-$3 nm) for the 0.2% NiO/NaTaO$_3$:La photocatalyst. The XPS survey spectrum for the 0.2% NiO/NaTaO$_3$:La photocatalyst is presented in Figure 3. The surface region consists primarily of Na, La, O, and Ta.
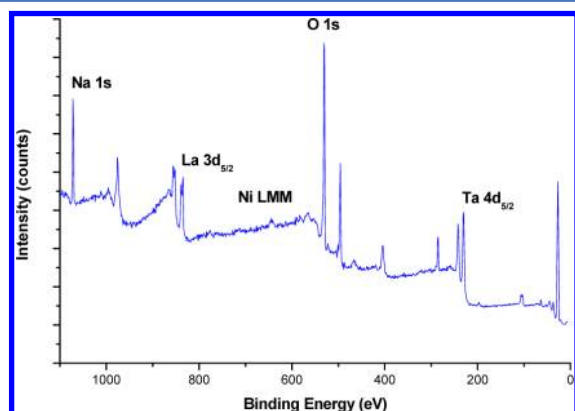
Figure 3. XPS survey spectrum of the surface region (1$-$3 nm) of the promoted 0.2% NiO/NaTaO$_3$:2% La photocatalyst. Only the primary XPS peaks are labeled because these peaks were employed in elemental quantification of the surface region.

The main XPS binding energy peak for nickel (Ni 2p$_{3/2}$) is not detected because of the overlap with the strong La 3d XPS binding energy peak. The appearance of the Ni LMM Auger peak confirms that Ni is indeed present in the surface region, but the amount cannot be directly quantified because of the overlap of the Ni 2p$_{3/2}$ peak with the La 3d peak. The atomic concentrations of the elements in the surface region are listed in Table 3. The relative sensitivity factor for the Ni LMM Auger

**Table 3. XPS Surface Region Atomic Concentrations of the Promoted 0.2% NiO/NaTaO$_3$:2% La Photocatalyst**

elemental core electron	atom % concentration
Na 1s	10.3
Ta 4d$_{5/2}$	13.4
O 1s	71.6
La 3d$_{5/2}$	3.7
Ni 2p$_{3/2}$[a]	1.0

[a]Estimated from Ni LMM using the NiO standard for determining the relative sensitivity factor.

peak with respect to the main XPS Ni 2p$_{3/2}$ peak was obtained using a NiO standard. This value was then used to estimate the XPS Ni 2p$_{3/2}$ peak area of NiO/NaTaO$_3$:La from the obtained Ni LMM Auger peak area. The 1.0% atomic concentration of Ni in the surface region is $\sim$5-fold higher than in the entire photocatalyst, which shows that Ni is enriched in the surface. The overall atomic concentration for lanthanum in the photocatalyst is 0.4%, and its 3.7% concentration in the surface region reveals that La is enriched in the surface by $\sim$9-fold in the NiO/NaTaO$_3$:La photocatalyst system.

3.5. High-Sensitivity Low-Energy Ion Scattering Spectroscopy.
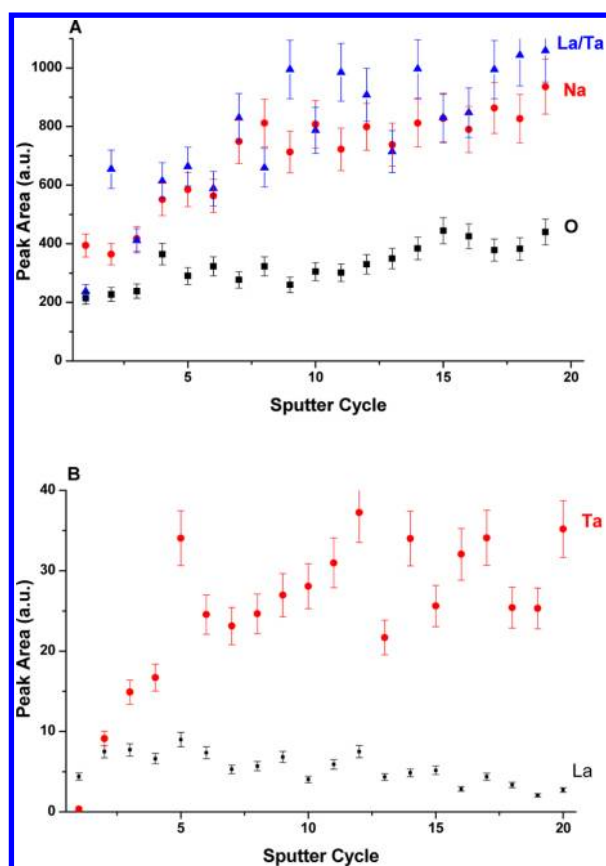
The atomic composition of the outermost surface layer ($\sim$0.3 nm) of the 0.2% NiO/NaTaO$_3$:2% La photocatalyst was determined by HS-LEIS. The HS-LEIS spectra for the outermost layer of the 0.2% NiO/NaTaO$_3$:2% La photocatalyst, using both He$^+$ and Ne$^+$ ion gases, are shown in Figure 4. For the He$^+$ HS-LEIS spectrum, scattering from
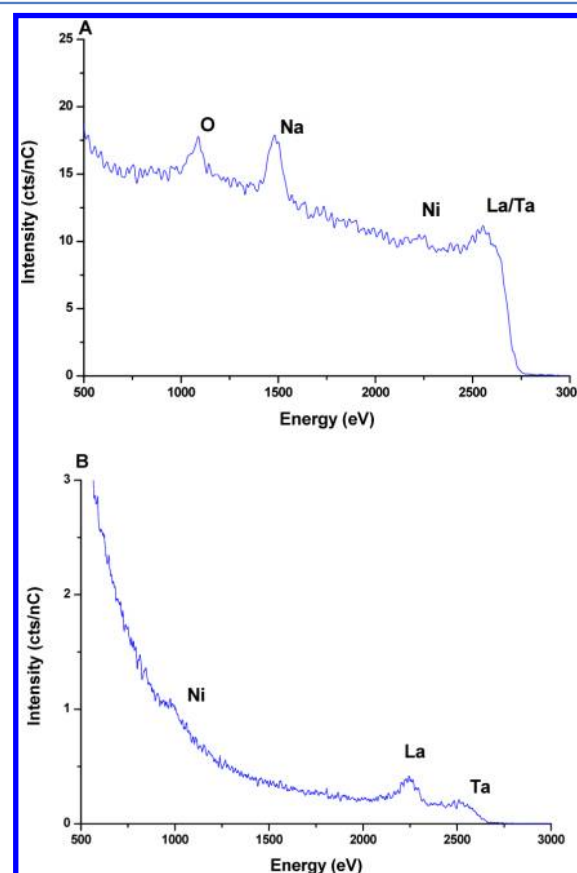
Figure 4. HS-LEIS spectra of the outermost surface layer ($\sim$0.3 nm) for the promoted 0.2% NiO/NaTaO$_3$:2% La photocatalyst using (A) He$^+$ ion gas and (B) Ne$^+$ ion gas.

Na, O, and Ni atoms with a low atomic mass is detected in the topmost surface layer, but the light He$^+$ ions cannot readily distinguish between the higher-atomic mass elements of La (139 amu) and Ta (181 amu). With the heavier Ne$^+$ ions, the La and Ta LEIS peaks can readily be resolved, and both elements are also found to be present on the topmost surface layer of the NiO/NaTaO$_3$:La photocatalyst.

HS-LEIS depth profiling analysis of the NiO/NaTaO$_3$:La photocatalyst was undertaken to determine the elemental compositional trends with distance from the outermost surface, and the findings are presented in Figure 5 (the raw spectra are presented in Figure S2 of the Supporting Information). Both O and Na signals are present on the outermost surface layer, and their concentrations further increase with the depth below the outermost surface as indicated in Figure 5A. The very weak and broad HS-LEIS Ni peak prevented its quantification. The Ni HS-LEIS signal is found to be present only in the first few sputtering cycles, revealing that Ni is concentrated within the outermost surface layers. The La HS-LEIS depth profile signal shown in Figure 5B demonstrates that La is present in the outermost surface layers and its level monotonically decreases with sputtering, reflecting its surface segregation. The appearance of a small La peak at the end of the sputtering

Figure 5. HS-LEIS elemental peak areas for the promoted 0.2% NiO/NaTaO$_3$:2% La photocatalyst during depth profile using (A) He$^+$ ion gas and (B) Ne$^+$ ion gas.

molecular structure of the NaTaO$_3$ photocatalysts is not perturbed by the addition of the La$_2$O$_3$ and NiO promoters because the pure NaTaO$_3$ and promoted NaTaO$_3$ photocatalysts exhibit the same Raman spectra of the bulk structure. Previous XRD characterization showed that the addition of La$_2$O$_3$ causes small shifts in the lattice constant of NaTaO$_3$ because of the substitution of minor amounts of La ions for Na ions in the bulk phase.[11] The addition of La also results in slightly more ordered crystals as previously reported[11] and is reflected in the slightly sharper Raman bands (see Figure 1). The bulk electronic structure of the NaTaO$_3$ photocatalysts is not perturbed by the addition of the La$_2$O$_3$ and NiO promoters because the pure NaTaO$_3$ and promoted NaTaO$_3$ photocatalysts possess the same optical band gap value of ~4.2 eV. The similar bulk molecular and electronic structures of the NaTaO$_3$ photocatalysts suggest that the La$_2$O$_3$ and NiO promoters are only minimally incorporated into the bulk NaTaO$_3$ lattice.

4.2. Surface Composition of the Promoted NaTaO$_3$ Photocatalyst. The HS-LEIS analysis of the outermost surface layer (~0.3 nm) of the promoted 0.2% NiO/NaTaO$_3$:La photocatalyst shows the presence of O, Na, Ni, and La. HS-LEIS depth profile analysis demonstrates that both La and Ni are surface segregated in the promoted NaTaO$_3$ photocatalyst because their concentrations decrease during depth profiling. The complete loss of the Ni HS-LEIS signal after a few sputtering cycles reflects that its concentration is limited to the outermost surface layers. HR-XPS analysis indicates that the La and Ni are enriched by factors of ~9- and ~5-fold in the surface region (~1−3 nm), respectively. Although some Na is present in the outermost surface layer of the promoted 0.2% NiO/NaTaO$_3$:La photocatalyst, HS-LEIS depth profiling indicates that its concentrations are not higher at the surface because the intensity of its HS-LEIS signal increases with depth profiling. Although Ta is not present on the outermost surface, the magnitude of the Ta HS-LEIS signal significantly increases with depth profiling, reflecting its depletion in the surface region. The only element whose concentration remains somewhat constant is O, which reflects the oxide nature of the promoted 0.2% NiO/NaTaO$_3$:La photocatalyst. The surface segregation of NiO and La$_2$O$_3$ in the promoted 0.2% NiO/NaTaO$_3$:La photocatalyst is consistent with the synthesis methods employed.

The promoted 0.2% NaTaO$_3$:La photocatalyst was synthesized by the solid-state method from physically mixed Ta$_2$O$_5$, Na$_2$CO$_3$, and La$_2$O$_3$ at elevated temperatures (1170−1420 K). Under these conditions, Ta$_2$O$_5$ reacts with Na$_2$CO$_3$ to form bulk NaTaO$_3$ because the molten state of basic Na at such extreme temperatures readily reacts with the acidic Ta$_2$O$_5$.[29,32] The molten basic Na does not have an affinity for reacting with the basic La$_2$O$_3$, and the low mobility of La$_2$O$_3$ (melting point

indicates that a low concentration of La may also be present in the bulk 0.2% NiO/NaTaO$_3$:La photocatalyst. In contrast, the HS-LEIS signal for Ta is small in the outermost surface layer and its level monotonically increases with sputtering, reflecting its diminished concentration on the outermost surface and in the surface region. Unlike those of Ta, the HS-LEIS spectra reveal that some Na is present on the outermost surface and that its concentration increases with sputtering. Perovskite ABO$_3$ structures have been shown to be preferentially enriched in the surface with the A cation (Na) and depleted in the surface of the B cation (Ta),[29−31] which is qualitatively consistent with the HS-LEIS depth profiling measurements obtained for the promoted NaTaO$_3$ in this study.

4. DISCUSSION

4.1. Bulk Molecular and Electronic Structures of NaTaO$_3$ Photocatalysts. The NaTaO$_3$ bulk phase has a perovskite structure with ABO$_3$ stoichiometry.[24] The bulk

Table 4. Photoactivities of Tantalum Oxide Photocatalysts for Water Splitting with UV Excitation at >270 nm

photocatalyst	BET (m^2/g)	TOR$_m$ (μmol of H$_2$ g^{-1} h^{-1})	TOR$_s$ (μmol of H$_2$ m^{-2} h^{-1})	N_s (no. of surface sites/g)	turnover frequency (s^{-1})
Ta$_2$O$_5$[a]	4 ± 0.1	6.0 × 10^0	1.5 × 10^0	−	−
1.0% NiO/Ta$_2$O$_5$[a]	4 ± 0.1	1.2 × 10^3	2.9 × 10^2	−	−
NaTaO$_3$[b]	0.44 ± 0.1	1.7 × 10^2	3.9 × 10^2	−	−
0.05% NiO/NaTaO$_3$[b]	0.44 ± 0.1	2.2 × 10^3	5.0 × 10^3	1.0 × 10^{18}	3.6 × 10^{-1}
NaTaO$_3$:2% La[b]	3.2 ± 0.1	4.5 × 10^2	1.4 × 10^2	1.3 × 10^{18}	5.8 × 10^{-2}
0.2% NiO/NaTaO$_3$:2% La[b]	3.2 ± 0.1	2.0 × 10^4	6.2 × 10^3	4.0 × 10^{18}	8.2 × 10^{-1}

^{a}From ref 7. ^{b}From ref 11.

of 2588 K) at these temperatures limits the reaction between acidic Ta_2O_5 and basic La_2O_3. Consequently, La_2O_3 is not extensively incorporated into the bulk $NaTaO_3$ structure and remains concentrated in the surface region and the topmost surface layer of the promoted $NaTaO_3$:La photocatalyst. Lanthanum oxide is also well-known to be a good additive for inhibiting particle sintering at high temperatures, resulting in an increased BET surface area and stabilization of small particles.[33,34] The promotion of $NaTaO_3$ with La_2O_3 resulted in an ~7-fold increased BET surface area (see Table 4), with much smaller and more ordered $NaTaO_3$ particles with characteristic nanostep morphology.[11] Previous TEM characterization showed that La was possibly responsible for the darker contrast at the edge of the crystal in the TEM image of $NaTaO_3$:5% La, and EDS analysis showed that La was more concentrated at the edge and grooves of the nanosteps than in the bulk.[11] This was observed for all $NaTaO_3$:La photocatalysts regardless of La loading, and it was concluded that La_2O_3 was localized near the surface. These findings are in agreement with the findings in this study that La_2O_3 is enriched at the surface.

The NiO promoter was added by subsequent impregnation of aqueous $Ni(NO_3)_2 \cdot 6H_2O$, drying, and calcination at 540 K for only 1 h. This mild calcination treatment is not sufficient to prompt a solid-state reaction between NiO and the bulk $NaTaO_3$:La phase, and consequently, Ni is also surface segregated in the promoted 0.2% $NiO/NaTaO_3$:La photocatalyst (see Table 3 and Figures 3 and 4). The EXAFS spectrum of 0.2% $NiO/NaTaO_3$:La does not exhibit the Ni−Ni (oxide) shell in its second coordination sphere, suggesting that Ni is present as an atomically dispersed species.[11] This is further supported by UV−vis d−d bands at ~580 and ~690 nm for 0.2% $NiO/NaTaO_3$:La that are characteristic of dispersed NiO species on oxide supports.[11] The highly dispersed nature of NiO present for 0.2% $NiO/NaTaO_3$ was also the conclusion of Kudo et al. because NiO particles could not be observed in the TEM images, and it was proposed that NiO is present as amorphous particles or dispersed species.[11] Thus, NiO is atomically dispersed in the outermost surface layers of the 0.2% $NiO/NaTaO_3$:La photocatalyst.

The atomically dispersed NiO species are most probably responsible for the sustained photoactivity of 0.2% $NiO/NaTaO_3$:La as a function of time during water splitting.[11] At higher NiO loadings (>0.5%) and with low-surface area La-free $NaTaO_3$, crystalline NiO particles can be observed in TEM images, and these photocatalysts are deactivated with reaction time. The deactivation was found to be accompanied by leaching of the active NiO component. This behavior suggests that stable $NiO/NaTaO_3$ photocatalysts require the presence of highly dispersed NiO species embedded in the outermost surface layers of $NaTaO_3$ and the absence of crystalline NiO particles.

4.3. Model of the Bulk and Surface Structures of the Promoted 0.2% $NiO/NaTaO_3$:La Photocatalyst.

As indicated above by XRD[11] and Raman characterization, the bulk structure of $NaTaO_3$:La consists of a perovskite ABO_3 structure with a minor amount of La substituted for Na. The addition of La during the photocatalyst synthesis results in smaller, more ordered crystallites that exhibit characteristic nanostep morphology. Surface analysis by HR-XPS and HS-LEIS spectroscopy reveals that the 0.2% $NiO/NaTaO_3$:La photocatalyst is enriched at the surface with Ni and La while being depleted at the surface of Na and Ta. The surface concentration of Na, however, is greater than that of Ta in the surface region.

The Ni is limited to the outermost surface layers and does not migrate into the bulk, while La is concentrated in the surface region and has also slightly migrated into the bulk. On the basis of these findings, a schematic of the bulk and surface structures of the promoted 0.2% $NiO/NaTaO_3$:La photocatalyst is depicted in Figure 6.
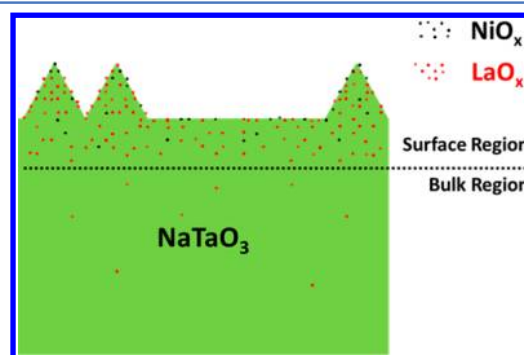
Figure 6. Schematic diagram of the surface region and bulk for the promoted 0.2% $NiO/NaTaO_3$:2% La photocatalyst.

It was previously proposed that NiO was preferentially deposited on the $NaTaO_3$:La nanostep structures as NiO particles based on TEM imaging.[11] It is important to note that the NiO particles could be detected with TEM for only ≥0.5% $NiO/NaTaO_3$:La, but NiO particles could not be detected for ≤0.2% $NiO:NaTaO_3$La. It was further proposed that the NiO particles are present as highly dispersed particles or species on the La-containing nanostep edge structures for 0.2% $NiO/NaTaO_3$:La.[11] The UV−vis d−d transitions[11] and the absence of the Ni−Ni shell in the EXAFS second coordination sphere for the supported NiO phase, however, reveal that NiO is present as dispersed species and not as NiO particles for the 0.2% $NiO/NaTaO_3$:La photocatalyst. The exact location of the dispersed NiO species for $NaTaO_3$:La is not known because no characterization method that can provide such two-dimensional distribution information for dispersed NiO species relative to La and Ta on the $NaTaO_3$:La photocatalyst currently exists. Given that NiO is present within the outermost surface layers and that both La and Ta are also present within the outermost surface layers, there is a high probability that dispersed NiO species are interacting with both La and Ta oxides for the 0.2% $NiO/NaTaO_3$:La photocatalyst.

4.4. Generation of Excited Electron−Hole Pairs and Their Lifetimes.

The main function of the bulk $NaTaO_3$ mixed oxide support phase is to control the material's optical band gap that generates excited electron−hole pairs and to supply them to the surface to allow the photocatalytic chemical reactions with water to take place. The same bulk $NaTaO_3$ structure and optical band gap for the unpromoted and promoted $NaTaO_3$ photocatalysts imply that the generation of electron−hole pairs by the bulk phase is the same for all the $NaTaO_3$ photocatalysts.

The recombination of excited electrons and holes is significantly affected by promotion of $NaTaO_3$ by the NiO and La_2O_3 additives, which are concentrated in the surface region, as reflected by their PL spectra (see Figure 2). The decrease in the intensity of the PL signal reflects the ability of the NiO and La_2O_3 promoters in the surface region to create efficient electron traps that help prevent electron−hole recombination and, thus, make the electrons and holes available

for photocatalysis.[35−37] The increase in the number of electron traps for La-promoted $NaTaO_3$, however, is partly related to the ~7-fold increase in surface area of the $NaTaO_3$:La photocatalytic material relative to that of unpromoted $NaTaO_3$ and possibly also to the promotion of La_2O_3. The increase in the number of electron traps with the NiO promoter directly reflects the photoproperties of NiO because the unpromoted photocatalyst and Ni-promoted photocatalyst exhibit the same surface area and particle sizes.

The decay part of the TR-PL spectra contains information about the lifetime of the excited electron−hole pairs, usually reflected by the slow t_2 component, and the $A_2/(A_1 + A_2)$ ratio is indicative of the relative population of these long-lived electrons with slow emission decay.[27,28] The addition of the efficient NiO electrons traps and the higher surface area of the La-promoted $NaTaO_3$ also dramatically diminish the relative contribution of the slow component of emission decay with a greater population of electrons with fast decay lifetimes. Although it is desirable for a photocatalyst to have a greater population of long-lived excited electrons with slow decay lifetimes, the trapping of the excited electrons by the surface NiO and the higher surface area allows more electrons and holes to perform photocatalysis at the oxide−water interface.

The effects of La_2O_3 and NiO on the dynamics of photoexcited electrons for the promoted $NaTaO_3$ photocatalyst have previously been examined with TR-IR spectroscopy.[16] It should be noted that TR-IR spectroscopy measures the IR absorbance of excited electrons (decay of excited electrons) while TR-PL measures PL emissions resulting from the recombination of excited electron−hole pairs (decay of electron−hole recombination). Furthermore, TR-PL measures recombination kinetics on a much shorter time scale (0.5−13 ns) than TR-IR (100 ns to 1 s), making direct comparisons between the two measurements somewhat difficult. The reaction kinetics measured with TR-IR (>100 ns), however, would be most comparable to the electron lifetimes reflected by the TR-PL slow component decay time constant (4−40 ns). The TR-PL measurements demonstrate that addition of La_2O_3 to $NaTaO_3$ lengthens the lifetime of the slow component electrons and, consequently, decreases the rate of decay of excited electrons that are detected by TR-IR spectroscopy. Addition of NiO to $NaTaO_3$:La shortens the lifetime of the TR-PL slow component electrons, while TR-IR findings indicate that addition of NiO increases the rate of decay of excited electrons, which was proposed to be due to the transfer of excited electrons from $NaTaO_3$:La to NiO.[11] This transfer occurred within 1 μs, and electrons were equilibrated between $NaTaO_3$:La and NiO between 1 μs and 1 s. Both TR-PL and TR-IR spectroscopy reveal that La_2O_3 is beneficial for increasing the lifetimes of excited electrons retarding the recombination kinetics of electron and holes on both experimental time scales (0.5−13 ns and 100 ns to 1 s), while NiO was found to be detrimental to the lifetimes of excited electrons. Although addition of NiO decreases the lifetime of excited electrons, TR-IR was able to show that there was still a population of excited electrons up to 1 s that can perform photocatalysis.

4.5. Structure−Activity Relationships for Splitting of H_2O by $NaTaO_3$ Photocatalysts.

The photocatalysis community typically reports photoactivity as mass-normalized TOR_m (moles of product per gram of photocatalyst per unit of time) that does not take into consideration variations in particle characteristics. Our findings for the promoted $NaTaO_3$

catalysts, however, demonstrate that the promoters are primarily altering the surface characteristics of the photocatalyst and suggest that the photoactivity should instead be normalized per unit surface area TOR_s (moles of product per square meter of photocatalyst per unit of time) and TOF [turnover frequency (number of molecules of product per photoactive surface site of photocatalyst per unit of time)] to account for structural and electronic changes of the photocatalyst.

The La_2O_3 promoter has been proposed to be an electronic promoter for the $NaTaO_3$ photocatalyst as the addition of La_2O_3 during the calcination synthesis was found to increase TOR_m by a factor of ~3. However when photoactivity is normalized by surface area, TOR_s is instead decreased by a factor of ~3 (see Table 4). Further increasing La_2O_3 loading results in an additional decrease in TOR_s (see Figure S3 of the Supporting Information). It appears that La_2O_3 actually inhibits photoactivity by occupying $NaTaO_3$ photocatalytic active sites. This indicates that La_2O_3 is not an electronic promoter but acts as a textural promoter that enhances the BET surface area by a factor of ~7. The increased surface area helps to compensate for the decrease in TOR_s with an increase in La_2O_3 loading.

The NiO additive, however, is an electronic promoter because it dramatically increases TOR_s by a factor of ~10−50 for $NaTaO_3$ in the presence and absence of the La_2O_3 promoter and does not affect the overall BET surface area or particle size of the photocatalyst (see Table 4 and Figure S4 of the Supporting Information). For the $NaTaO_3$:La photocatalyst, note that the dramatic enhancement of TOR_s by NiO occurs only when it is present as a dispersed species in the outermost surface layers of the 0.2% $NiO/NaTaO_3$:La photocatalyst. Higher NiO loading leads to the formation of crystalline NiO particles that appear to only slightly enhance TOR_s of 2.0% $NiO/NaTaO_3$:La and deactivate with reaction time (see Figure S4 of the Supporting Information). The activities of the 1.0% NiO/Ta_2O_5 and 0.05% $NiO/NaTaO_3$ photocatalysts decrease over time, suggesting that NiO particles are also not as stable as dispersed NiO species. Thus, it can be concluded that highly dispersed NiO species embedded in the surface region, and especially on the outermost surface layer, rather than the NiO particles are the catalytic active sites responsible for the enhanced photoactivity of 0.2% $NiO/NaTaO_3$:La materials.

In addition to normalizing activity by TOR_m and TOR_s, the reaction rates of some of the photocatalyst are also normalized by TOF, as is practiced in traditional thermal heterogeneous catalysis (see Table 4). Determination of TOF requires knowing the number of photocatalytic surface sites (N_s) that can be determined via surface analysis. The number of photocatalytic surface Ta sites (N_s) for $NaTaO_3$:2% La was estimated from HR-XPS analysis, and the number of photocatalytic surface Ni sites (N_s) for 0.05% $NiO/NaTaO_3$ and 0.2% $NiO/NaTaO_3$:2% La was estimated from HS-LEIS analysis (see Table 4 and the Supporting Information). The TOF photoactivity values for 0.05% $NiO/NaTaO_3$ and 0.2% $NiO/NaTaO_3$:2% La are comparable, only varying by ~2-fold, further confirming that La_2O_3 is only a textural promoter and not an electronic promoter.

The previously proposed model for the promoted 0.2% $NiO/NaTaO_3$:La photocatalyst invokes a synergistic interaction between the highly dispersed NiO that preferentially self-assembles at La-rich nanostep structures.[11] This conclusion was reached because the simultaneous addition of NiO and La_2O_3 to $NaTaO_3$ resulted in the extreme enhancement of the overall

photoactivity for water splitting. TEM was able to detect NiO particles for the 0.5% NiO/NaTaO$_3$:1.5% La photocatalyst when it was deposited on the La-rich nanostep structures. Furthermore, it was assumed that the highly dispersed NiO would also behave like the NiO particles by interacting with La at the nanosteps. There is no direct evidence, however, to confirm that the highly dispersed NiO species preferentially assemble at the La-rich nanostep structures for the highly active 0.2% NiO/NaTaO$_3$:2% La photocatalyst because the dispersed NiO component cannot be observed with TEM for this sample. Although the new surface characterization information can reveal that NiO is located on the outermost surface layers of 0.2% NiO/NaTaO$_3$:La, there is no supporting evidence that it is preferentially distributed on the La-rich nanostep structures. Furthermore, the NiO additive promotes the specific TOR$_s$ photoactivity for water splitting by a factor of ~10−50 with and without the La$_2$O$_3$ promoter, indicative of the absence of a synergistic interaction between the NiO and La$_2$O$_3$ components. The absence of promotion by La is reflected by the almost same TOR$_s$ values for the NaTaO$_3$ and NaTaO$_3$:La photocatalysts (see Table 4). The new model for the 0.2% NiO/NaTaO$_3$:La photocatalyst presented in Figure 6 is more realistic and is based on both supporting surface and bulk information that was not available in earlier studies.

5. CONCLUSIONS

The surface and bulk properties of promoted NiO/NaTaO$_3$:La photocatalysts were investigated via surface (HS-LEIS and HR-XPS) and bulk (Raman, UV−vis, and PL) spectroscopy. The bulk NaTaO$_3$ perovskite molecular and electronic structures are not affected by the La$_2$O$_3$ and NiO promoters, with only minor substitution of La for Na, which means that the bulk photogenerated excited electron−hole pairs are the same for all the NaTaO$_3$-based photocatalysts. Both promoters are surface-segregated on the NaTaO$_3$ particles. The La$_2$O$_3$ additive is only a structural promoter, stabilizing smaller NaTaO$_3$ particles and increasing the BET surface area (~7-fold). The NiO additive is a potent electronic promoter that dramatically increases the specific TOR$_s$ photoactivity for water splitting by a factor of ~10−50 and TOF by a factor of ~10 with and without the La$_2$O$_3$ promoter. The new surface findings provide additional fundamental molecular and electronic insights into the photocatalysis mechanism of promoted NiO/NaTaO$_3$:La photocatalysts by emphasizing the role of the surface catalytic active sites and the need to normalize the photoactivity per unit surface area. Reporting photocatalytic performance with surface active site-normalized TOF and surface area-normalized TOR$_s$ rates in addition to the typically reported TOR$_m$ provides for a deeper fundamental understanding of structural changes affecting the photocatalysis process of heterogeneous photocatalysts.

ASSOCIATED CONTENT

Ⓢ Supporting Information

PL emission decay curves for tantalum-based photocatalysts (Figure S1), HS-LEIS depth profile for the promoted 0.2% NiO/NaTaO$_3$:2% La photocatalyst using He$^+$ ion gas and Ne$^+$ ion gas (Figure S2), TOR$_s$ (micromoles of H$_2$ per square meter per hour) as a function of La loading for NaTaO$_3$:La (Figure S3), and TOR$_s$ (micromoles of H$_2$ per square meter per hour) as a function of Ni loading for NaTaO$_3$:2% La (Figure S4), and calculation of Ns from surface HR-XPS and HS-LEIS analysis.

This material is available free of charge via the Internet at http://pubs.acs.org.

AUTHOR INFORMATION

Corresponding Author
*E-mail: iew0@lehigh.edu.

Funding

Notes
The authors declare no competing financial interest.

REFERENCES

(1) Fujishima, A.; Honda, K. *Nature* **1972**, *238*, 37−38.
(2) Maeda, K.; Domen, K. *J. Phys. Chem. C* **2007**, *111*, 7851−7861.
(3) Osterloh, F. E. *Chem. Mater.* **2008**, *20*, 35−54.
(4) Kudo, A.; Miseki, Y. *Chem. Soc. Rev.* **2009**, *38*, 253−278.
(5) Chen, X.; Shen, S.; Guo, L.; Mao, S. S. *Chem. Rev.* **2010**, *110*, 6503−6570.
(6) Sayama, K.; Arakawa, H. *J. Photochem. Photobiol., A* **1994**, *77*, 243−247.
(7) Kato, H.; Kudo, A. *Chem. Phys. Lett.* **1998**, *295*, 487−492.
(8) Kato, H.; Kudo, A. *J. Phys. Chem. B* **2001**, *105*, 4285−4292.
(9) Kudo, A.; Kato, H. *Chem. Lett.* **1997**, 867−868.
(10) Kato, H.; Kudo, A. *Chem. Lett.* **1999**, 1207−1208.
(11) Kato, H.; Asakura, K.; Kudo, A. *J. Am. Chem. Soc.* **2003**, *125*, 3082−3089.
(12) Kudo, A.; Kato, H. *Chem. Phys. Lett.* **2000**, *331*, 373−377.
(13) Kudo, A.; Kato, H.; Tsuji, I. *Chem. Lett.* **2004**, *33*, 1534−1539.
(14) Merzlikin, S. V.; Tolkachev, N. N.; Briand, L. E.; Strunskus, T.; Woll, C.; Wachs, I. E.; Grunert, W. *Angew. Chem., Int. Ed.* **2010**, *49*, 8037−8041.
(15) Wachs, I. E.; Routray, K. *ACS Catal.* **2012**, *2*, 1235−1246.
(16) Yamakata, A.; Ishibashi, T.; Kato, H.; Kudo, A.; Onishi, H. *J. Phys. Chem. B* **2003**, *107*, 14383−14387.
(17) Mills, A.; Le Hunte, S. *J. Photochem. Photobiol., A* **1997**, *108*, 1−35.
(18) Kubelka, P.; Munk, F. *Z. Tech. Phys.* **1931**, *12*, 593−601.
(19) Gao, X.; Wachs, I. E. *J. Phys. Chem. B* **2000**, *104*, 1261−1268.
(20) Delgass, W. N. *Spectroscopy in Heterogeneous Catalysis*; Academic Press: New York, 1979.
(21) Selby, B. J.; Quickenden, T. I.; Freeman, C. G. *Kinet. Catal.* **2003**, *44*, 5−15.
(22) Quickenden, T. I.; Green, T. A.; Lennon, D. *J. Phys. Chem.* **1996**, *100*, 16801−16807.
(23) Chen, Y.; Fierro, J. L. G.; Tanaka, T.; Wachs, I. E. *J. Phys. Chem. B* **2003**, *107*, 5243−5250.
(24) Teixeira, N. G.; Dias, A.; Moreira, R. L. *J. Eur. Ceram. Soc.* **2007**, *27*, 3683−3686.
(25) Burns, G.; Dacol, F. *Phys. Rev. B* **1990**, *41*, 4747−4748.
(26) Chan, S. S.; Wachs, I. E. *J. Catal.* **1987**, *103*, 224−227.
(27) Tang, J.; Durrant, J. R.; Klug, D. R. *J. Am. Chem. Soc.* **2008**, *130*, 13885−13891.
(28) Roberts, C. A. Fundamental Structure-Activity Relationships of TiO$_2$-Based Photocatalysts. Ph.D. Dissertation, Lehigh University, Bethlehem, PA, 2012.

(29) Kilner, J. A.; Skinner, S. J.; Brongersma, H. H. *J. Solid State Electrochem.* **2011**, *15*, 861−876.

(30) Fullarton, I. C.; Jacobs, J.-P.; Benthem, H. E.; Kilner, J. A.; Brongersma, H. H.; Scanlon, P. J.; Steele, B. C. H. *Ionics* **1995**, *1*, 51−58.

(31) Viitanen, M. *Solid State Ionics* **2002**, *150*, 223−228.

(32) Brongersma, H.; Draxler, M.; Deridder, M.; Bauer, P. *Surf. Sci. Rep.* **2007**, *62*, 63−109.

(33) Church, J. S.; Cant, N. W.; Trimm, D. L. *Appl. Catal., A* **1993**, *101*, 105−116.

(34) Ferrandon, M. *J. Catal.* **2001**, *200*, 148−159.

(35) Anpo, M.; Kamat, P. V. *Environmentally Benign Photocatalysts: Applications of Titanium Oxide-based Materials*; Springer: New York, 2010.

(36) Hu, C.; Tsai, C.; Teng, H. *J. Am. Ceram. Soc.* **2009**, *92*, 460−466.

(37) Hu, C.; Lee, Y.; Teng, H. *J. Mater. Chem.* **2011**, *21*, 3824−3830.